






Article

Nickel-Doped Ceria Bifunctional Electrocatalysts for Oxygen Reduction and Evolution in Alkaline Media

Jadranka Milikić¹, Rodolfo O. Fuentes², Julia E. Tasca³, Diogo M. F. Santos^{4,*}, Biljana Šljukić^{1,4}
and Filipe M. L. Figueiredo^{5,*}¹ University of Belgrade, Faculty of Physical Chemistry, Studentski trg 12–16, 11158 Belgrade, Serbia² Instituto de Nanociencia y Nanotecnología, Departamento de Física, Centro Atómico Constituyentes, CNEA-CONICET, Av. Gral. Paz 1499, San Martín, Buenos Aires B1650, Argentina³ CIFICEN (UNCPBA-CICPBA-CONICET), Facultad de Ingeniería–UNCPBA, Av. Del Valle 5737, Olavarría B74001WI, Argentina⁴ Center of Physics and Engineering of Advanced Materials (CeFEMA), Laboratory for Physics of Materials and Emerging Technologies (LaPMET), Chemical Engineering Department, Instituto Superior Técnico, Universidade de Lisboa, 1049–001 Lisbon, Portugal⁵ CICECO, Physics Dept., University of Aveiro, Campus Universitário de Santiago, 3810–193 Aveiro, Portugal

* Correspondence: diogosantos@tecnico.ulisboa.pt (D.M.F.S.); lebre@ua.pt (F.M.L.F.)

Abstract: Nickel-doped ceria ($\text{Ce}_{1-x}\text{Ni}_x\text{O}_{2-\delta}$) nanopowders (7 to 5 nm in size) synthesized by the cation complexation method with 5, 10, 15, and 20 Ni at.% are studied with respect to their electrochemical activity for the oxygen reduction (ORR) and oxygen evolution (OER) reactions in alkaline medium. One finds good bifunctional electrocatalytic activity of the four $\text{Ce}_{1-x}\text{Ni}_x\text{O}_{2-\delta}$ electrocatalysts. The Tafel analysis of the ORR in the 0.57–0.78 V vs. RHE potential window leads to slopes in the 70–108 mV dec^{-1} range. The number of electrons exchanged during ORR is between 2 and 2.7. The OER Tafel slopes are determined to be in the range 192–281 mV dec^{-1} . OER activation energies are found to range between 28 and 43 kJ mol^{-1} . The specific capacitance of $\text{Ce}_{1-x}\text{Ni}_x\text{O}_{2-\delta}$ electrocatalysts measured at a scan rate of 100 mV s^{-1} varies between 0.7 and 1.4 Fg^{-1} . The results demonstrate that $\text{Ce}_{1-x}\text{Ni}_x\text{O}_{2-\delta}$ nanopowders can act as bifunctional electrocatalysts for ORR/OER for potential application in the oxygen electrode of devices such as rechargeable metal–air batteries.

Keywords: nickel-doped ceria; oxygen reduction reaction; oxygen evolution reaction; rechargeable metal–air batteries



Citation: Milikić, J.; Fuentes, R.O.; Tasca, J.E.; Santos, D.M.F.; Šljukić, B.; Figueiredo, F.M.L. Nickel-Doped Ceria Bifunctional Electrocatalysts for Oxygen Reduction and Evolution in Alkaline Media. *Batteries* **2022**, *8*, 100. <https://doi.org/10.3390/batteries8080100>

Academic Editor: Seung-Tae Hong

Received: 24 July 2022

Accepted: 17 August 2022

Published: 19 August 2022

Publisher's Note: MDPI stays neutral with regard to jurisdictional claims in published maps and institutional affiliations.



Copyright: © 2022 by the authors. Licensee MDPI, Basel, Switzerland. This article is an open access article distributed under the terms and conditions of the Creative Commons Attribution (CC BY) license (<https://creativecommons.org/licenses/by/4.0/>).

1. Introduction

Electrochemical energy conversion and storage devices present a high potential for various applications as they can be more environmental-friendly than fossil fuel-based conventional systems [1]. Most of today's research on these electrochemical devices aims to find inexpensive, efficient, and selective catalysts for the anodic and cathodic reactions to increase their efficiency [2–9]. Central reactions in electrochemical energy conversion and storage systems, such as fuel cells, water electrolyzers, or metal–air batteries, are the oxygen reduction (ORR) and oxygen evolution (OER) reactions. Rechargeable metal–air batteries require bifunctional ORR/OER catalysts as ORR proceeds during discharging, with the reverse process, i.e., OER, proceeding during charging [10–12]. Generally, metal–air batteries are very practical due to their high energy densities ranging from 350 to 1700 Wh kg^{-1} , low weight, and economic viability as they use O_2 from the air [10,13,14]. Thus, Li- and Zn-air batteries are widely tested and seen as an alternative to Li-ion batteries for application in electric vehicles and other electric devices [10,15]. Pt/C, Pd/C, Ru, Ir, and its alloys have been explored and pointed out as the most promising electrocatalysts for ORR and OER reactions [16,17]. Namely, Pt demonstrates the best performance for ORR, and it is typically supported on carbon (Pt/C), showing high activity in terms of produced current and high selectivity for the complete four-electron reduction of O_2 [18,19].

However, all these noble metal-based electrocatalysts are expensive and their intrinsic rarity may compromise future mass deployment of the technology. For this reason, oxygen electrode reaction electrocatalysis in alkaline media is generally preferred, as it may allow the use of lower-cost noble metal-free electrocatalysts.

ORR in alkaline media can proceed by two pathways: a direct four-electron pathway or a two-electron peroxide (HO_2^-) pathway. During the four-electron pathway, molecular O_2 is directly reduced to H_2O or OH^- , and through the two-electron peroxide pathway, molecular O_2 is first reduced to HO_2^- and then to H_2O [20]. The direct and peroxide ORR mechanisms in alkaline media are described in Equations (1) and (2), respectively.



The HO_2^- ion formed during 2e^- -ORR in alkaline medium can be further reduced by Equation (3).



The ORR pathway is, to a great extent, determined by the cathode material. Despite the high selectivity and activity of Pt, its high price requires the replacement of benchmark Pt/C by alloy electrocatalysts containing lower amounts of this noble metal or, ideally, by non-noble metal electrocatalysts.

On the other hand, OER is carried out at the anode side of certain electrolytic processes, releasing four electrons and, in alkaline media, is represented by the reverse of Equation (1) [21]. Ni electrodes are typically used for OER in water electrolyzers in alkaline media due to their good stability and resistivity to corrosion [22,23]. While Pt-based and Ni-based materials show activity for ORR and OER, respectively, their activity for the reverse reaction is typically lower, suggesting the need for developing bifunctional ORR/OER catalysts. Interesting two-dimensional (2D) materials have revealed competitive electrochemical activity, namely transition metal carbides/nitrides with related MXene structure [24]. While such kind of 2D catalysts may indeed offer competitive performance, design and synthesis issues related to their metastability represent serious challenges for their development [25]. More conventional metal oxides with a 3D nanoparticle morphology that can be synthesized by simpler, low-cost methods may be a more attractive and stable solution upon identification of suitable compositions.

Indeed, metal oxides, such as cerium oxide (CeO_x), have potential application in fuel cells, offering several benefits that include higher corrosion resistance compared to carbon supports. When used as supports or co-catalysts, metal oxides strongly interact with metal particles, thus preventing their agglomeration. Furthermore, these oxides can influence electronic properties and modify the electrocatalytic activity of the metal. Finally, metal oxides have abundant hydroxyl groups on their surfaces, which can work as co-catalysts of noble metal catalysts based on bifunctional mechanisms [26].

References to Ni-doped ceria ($\text{Ce}_{1-x}\text{Ni}_x\text{O}_{2-\delta}$) as a catalyst are mostly centered on high-temperature applications such as methane dry reforming or oxidation [27,28], ethanol steam reforming [29], CO oxidation [30], water gas shift reaction [31], or as a coking-resistant functional layer in the anodes of solid oxide fuel cells [32].

To the best of our knowledge, there are no reports of the electrocatalytic activity of $\text{Ce}_{1-x}\text{Ni}_x\text{O}_{2-\delta}$ for the OER or ORR at low temperature, neither in alkaline nor acidic media. In a close application context, Tan et al. communicated the positive effect (in comparison to pure CeO_2) of nickel-doped ceria nanoparticles for promoting the catalytic activity of Pt/C for ethanol electrooxidation in acidic medium due to a positive effect of $\text{Ce}_{1-x}\text{Ni}_x\text{O}_{2-\delta}$ in removing poisoning intermediates adsorbed on Pt [33]. Parwaiz et al. demonstrated high ORR activity of 3 at.% cobalt-doped ceria/reduced graphene oxide nanocomposites through the creation of more active sites in comparison to the equivalent formulation containing pure ceria [34]. Yang et al. also reported on the intrinsic electrocatalytic activity of Co-doped

CeO₂ (up to 25 at.%) for both ORR and OER in alkaline medium [35]. The authors detected a remarkable improvement in the activity of ceria doped with 20 at.% Co associated with a decrease in charge transfer impedance, which they ascribe to increased electronic conductivity, increased active oxygen species, and increased oxygen vacancy concentration (interestingly, the fraction of trivalent Ce is similar for CeO₂ and Ce_{0.80}Ni_{0.20}O_{2-δ}). Investigation of electrocatalytic activity and stability of Pd-CeO₂-nanorods on carbon (Pd-CeO₂-NR/C) for the ORR in alkaline conditions showed that ORR at Pd-CeO₂-NR/C proceeds with transfer of four electrons and low H₂O₂ production (ca. 2–4%) [36]. Moreover, this material exhibited higher mass and specific activity than Pd/C, evidencing that the presence of CeO₂-NR improves the electrocatalytic performance of Pd for the ORR [36]. Similarly, Pd–Ag alloy-supported on mesoporous CeO₂ showed superior electrocatalytic activity and stability for the ORR in alkaline media [37]. The excellent activity toward ORR was attributed to the high surface area of CeO₂ large number of active sites provided by the presence of Pd–Ag alloy (20 wt.%) [37]. Cerium-doped cobalt oxide (CoO_x(Ce)) showed superior OER activity than a commercial noble metal electrocatalyst (RuO₂) and CoO_x in 1 M KOH [38]. CoO_x(Ce) showed smaller activation energy and 2.7 times higher electrochemical surface area (ECSA) than CoO_x [38]. CeO₂ on biochar carbon (CeO₂/BC (at 700, 800, and 900 °C)) materials were synthesized by simple one-pot hydrothermal treatment and were examined for ORR in alkaline media [39]. The CeO₂/BC700 catalysts showed the highest ORR activity with the highest j_k (at 0.7 V) value of 3.4 mA cm⁻² [39]. Three types of Pd–CeO₂/C catalysts showed activity for hydrogen oxidation reaction (HOR) in alkaline media where Type 1 and Type 3 catalysts show higher stability than Pd supported on carbon black [40]. Cerium oxide (CeO_{2-δ}) ultrafine nanoparticles were used as anchoring sites for the polymerization of aniline [41]. The synthesized materials showed higher capacitance (299 F g⁻¹ and 314 F g⁻¹) than polyaniline-emeraldine salt (294 F g⁻¹) [41].

Fuentes et al. previously studied the solubility limit and redox properties of Ce_{1-x}Ni_xO_{2-δ} (x = 0.05, 0.10, 0.15, and 0.20) nanopowders using a combination of electron microscopy, synchrotron radiation X-ray diffraction (SR-XRD) and X-ray absorption near-edge spectroscopy (XANES) [42]. Analogously to cobalt-doped ceria, the Ni doping also creates oxygen vacancies and enhances the electronic conductivity of ceria, facilitating charge transfer processes with a potentially positive impact on the electrochemical activity. The present work attempts to assess the potential of these materials as bifunctional electrocatalysts for the ORR and OER in alkaline medium based on a battery of electrochemical tests, including cyclic voltammetry (CV), linear scan voltammetry with rotating disk electrode (LSV RDE), electrochemical impedance spectroscopy (EIS), and chronoamperometry (CA)

2. Results

2.1. General Properties of the Ce_{1-x}Ni_xO_{2-δ} Powders

Table 1 summarizes the properties of the powders used in the present electrochemical study, as detailed in reference [42] to our previous work. All the Ce_{1-x}Ni_xO_{2-δ} (x=0.05, 0.10, 0.15, and 0.20) compositions were found to have a cubic crystal structure (Fm3m space group), as revealed by synchrotron radiation powder X-ray diffraction (SR-XRD, Figure S1 in Supplementary Information). This technique detects traces of a segregated NiO phase for nominal Ni contents higher than 15 at.%, thus indicating this to be the solubility limit in ceria nanocrystals with ca. 5 nm of equivalent diameter. It should be noticed that such a level of solubility is only achieved for nanopowders with a typical crystallite size of less than 10 nm. Indeed, the large difference in ionic radius and coordination number between Ni²⁺ and the cerium cations Ce⁴⁺ and Ce³⁺ leads to substantial structural perturbation of the host lattice that precludes doping levels higher than 1 at.% in conventional micron-sized powders [42]. At room temperature, the lattice parameter of the Ce_{1-x}Ni_xO_{2-δ} mixed oxide nanopowder increases with the Ni content. Since the ionic radius of Ni²⁺ (^{VI}r_{Ni}²⁺=0.69 Å) is much smaller than that of either Ce⁴⁺ or Ce³⁺ (^{VIII}r_{Ce}⁴⁺=0.97 Å, ^{VIII}r_{Ce}³⁺=1.14 Å) [43], one may conclude that the lattice expansion is not directly related to differences in ionic radii between the dopant and the host cations. Another explanation for the lattice expansion

could be the partial reduction of tetravalent cerium cations to the larger trivalent counterparts. Still, the X-ray absorption near-edge spectroscopy (XANES) data indicate a nearly constant $\text{Ce}^{3+}:(\text{Ce}^{3+}+\text{Ce}^{4+})$ ratio at room temperature across the entire compositional series. Therefore, the slight lattice expansion observed in the room temperature SR-XRD patterns indicates a dominant effect of the formation of oxygen vacancies, which are the most likely species to balance the positive charge of the defects resulting from the substitution of Ce^{4+} by Ni^{2+} ($\text{Ni}_{\text{Ce}^{4+}}^{\bullet\bullet}$, in Kröger–Vink notation).

Table 1. Lattice parameter (a), phase composition, average crystallite size (D_{XRD}), specific surface area (S_{BET}), derived equivalent spherical diameter (D_{BET}), and pore volume of the $\text{Ce}_{1-x}\text{Ni}_x\text{O}_{2-\delta}$ powders [42].

x in $\text{Ce}_{1-x}\text{Ni}_x\text{O}_{2-\delta}$	a (Å)	%(Ce,Ni)O ₂ : %NiO	D_{XRD} (nm)	S_{BET} (m ² g ⁻¹)	D_{BET} (nm)	$D_{\text{BET}}:D_{\text{XRD}}$	Pore Volume (cm ³ g ⁻¹)
0	5.4144(6)	—	11.9	26	35	2.9	—
0.05	5.4150(6)	100:0	7.1	39	22	3.1	0.070
0.10	5.4149(6)	100:0	5.9	37	24	4.1	0.048
0.15	5.4163(3)	98:2	5.6	31	29	5.2	0.040
0.20	5.4173(2)	96:4	5.0	35	26	5.2	0.044

To understand the dominant functional groups present in the nanostructured nickel-doped ceria oxides with different Ni content, Fourier transform infrared spectra (FTIR) were recorded at room temperature, including the non-substituted CeO_2 as reference (Figure S2 in Supplementary Information). The formation of cerium oxide is confirmed in these spectra since the frequency of Ce-O has reached below 400 cm^{-1} for all samples, with the shoulder at 550 cm^{-1} ascribed as a characteristic phonon mode for cubic CeO_2 . Moreover, the small shoulder at 630 cm^{-1} , present only in the Ni-doped CeO_2 samples, is attributed to modifications of the oxygen sublattice due to the introduction of nickel into the ceria network, confirming the modification of the M-O bonding symmetry and the formation of the Ni-Ce-O solution. On the other hand, the small intensity peak at 1384 cm^{-1} is assigned to the existence of stretching vibration bands of NO_3^- ion, indicating that the nitrates are not decomposed completely into oxides. This signal is greater as the content of Ni increases, which suggests that the nickel content would delay the decomposition of the precursor. Finally, the signal located at 285 cm^{-1} for $\text{Ce}_{0.95}\text{Ni}_{0.05}\text{O}_{2-\delta}$ is shifted to lower frequencies with respect to that of the other materials, thus indicating less force of bond Ce-O and probably less charge transport resistance.

The powders were also analyzed by low-resolution scanning transmission electron microscopy, which revealed that the nanocrystallites form aggregates with a foam-like microstructure where one can identify large spherical pores, with around $0.5\text{--}1\text{ }\mu\text{m}$, and other pores smaller than 100 nm (Figure S3 in Supplementary Information). High-resolution transmission electron microscopy confirms that the powder aggregates are indeed formed by nanometric powders with particle size well below 10 nm , in excellent agreement with the analysis of the SR-XRD patterns using the Scherrer equation (see Figures 6 and 7 in Ref. [42]). The latter results, shown in Table 1, indicate a slight decrease in the crystallite size with increasing dopant content, particularly noticeable between the undoped material (11.9 nm) and the series of Ni-containing samples (decreasing from 7.1 nm for $x = 0.05$ to 5.0 nm for $x = 0.2$). Table 1 also lists the specific surface area of the nanopowders, estimated through the Brunauer–Emmett–Teller method (BET), from nitrogen sorption isotherms at 77 K , which is higher for the doped materials than for pure ceria, thus indicating a higher level of agglomeration of the Ni-containing materials. Therefore, the corresponding equivalent spherical diameter of the $\text{Ce}_{1-x}\text{Ni}_x\text{O}_{2-\delta}$ particles is distinctly smaller than for CeO_2 . A comparison of these data with the average crystallite size estimated from the SR-XRD patterns, expressed through the $D_{\text{BET}}:D_{\text{XRD}}$ ratio (Table 1), further suggests that the level of agglomeration of the particles increases with increasing Ni content up to $x = 0.15$, remaining roughly the same for higher Ni content. The analysis of the desorption data using the Barrett–Joyner–Halenda method (BJH) revealed very similar pore size distributions for

all Ni-containing materials, featuring the existence of mesopores with an average diameter of around 3.3 nm (Figure S4 in Supplementary Information). The total pore volume tends to decrease with increasing Ni content, but differences are negligible between $x = 0.1$ and $x = 0.2$ (see Table 1).

2.2. Capacitance Study

The specific capacitance of the four studied materials in deaerated 0.1 M KOH was determined by integrating the anodic and cathodic halves of the CV curves obtained at different scan rates. Figure S5 in Supplementary Information illustrates the behavior of $\text{Ce}_{0.95}\text{Ni}_{0.05}\text{O}_{2-\delta}$ in deaerated 0.1 M KOH solution with scan rates increasing from 10 to 500 mV s^{-1} . CV curves were somewhat asymmetric and not rectangular as expected for typical electrical double-layer capacitors. This asymmetry is seen as a more pronounced slope of the curve in the negative scan direction and it is related to the pore diameter and, consequently, to the ability of electrolyte ions to penetrate into the catalyst pores. Still, the overall shape of CV curves for all studied materials was not affected by the change in the scan rate, demonstrating stable and reproducible capacitance behavior. As expected, the specific capacitance of the four materials decreases with increasing scan rate (Figure 1A), since the ions have less time to penetrate deeply into pores and therefore produce lower charges and lower specific capacitance, with such behavior being typical of electrolytic capacitors [44].

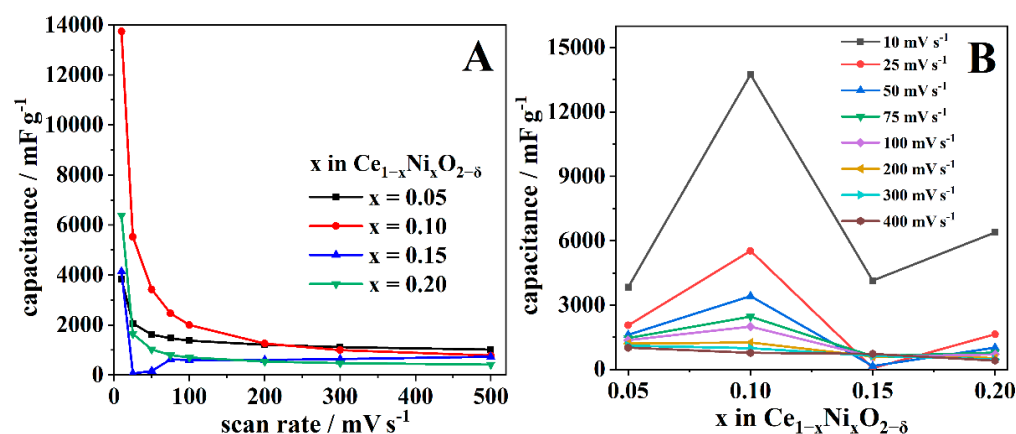


Figure 1. Specific capacitance values plotted as a function of the (A) potential scan rate and (B) electrode composition (lines are a guide for the eye).

The data show that the capacitance goes through a maximum for $x = 0.10$ (i.e., $\text{Ce}_{0.90}\text{Ni}_{0.10}\text{O}_{2-\delta}$) for scan rates lower than 300 mV s^{-1} (Figure 1B), which could be due to the aforementioned larger asymmetry in the CV observed for this particular sample. The particularity of the $\text{Ce}_{0.90}\text{Ni}_{0.10}\text{O}_{2-\delta}$ sample vanishes at high scan rates, where one observes a progressive decrease in capacitance with increasing Ni content. This is most likely due to the progressive increase in the samples' conductivity with increasing Ni-doping levels.

2.3. ORR Studies

ORR at different $\text{Ce}_{1-x}\text{Ni}_x\text{O}_{2-\delta}$ samples was systematically studied in O_2 -saturated 0.1 M KOH. Control CVs of all four materials recorded in deaerated 0.1 M KOH solutions showed a small peak at ca. 0.6 V corresponding to Ce (IV) reduction to Ce (III). Figure S6 in Supplementary Information illustrates the voltammetric response of $\text{Ce}_{0.95}\text{Ni}_{0.05}\text{O}_{2-\delta}$ in deaerated and O_2 -saturated 0.1 M KOH. CVs of the four electrodes in O_2 -saturated 0.1 M KOH solution show ORR onset potentials of 0.74, 0.73, 0.68, and 0.67 V for samples with $x = 0.05, 0.20, 0.15,$ and 0.10 , respectively (Figure 2A).

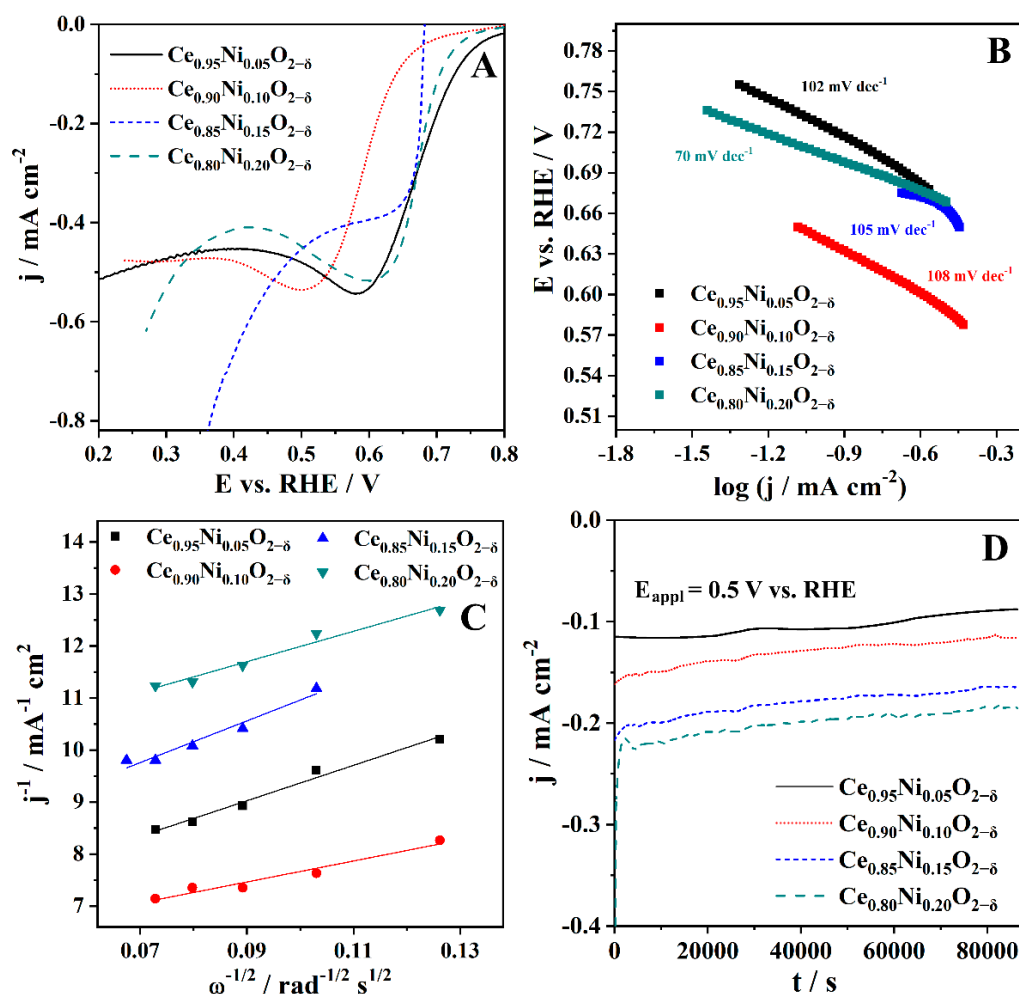


Figure 2. (A) CVs (cathodic scan) of the four studied materials recorded at a scan rate of 50 mV s^{-1} with the corresponding (B) Tafel slopes, (C) Koutecky–Levich plots, and (D) CA curves recorded for 24 h. All measurements performed in O_2 -saturated 0.1 M KOH . Potential values are corrected for the ohmic drop in the electrolyte.

These results demonstrate the activity of these materials for ORR, although the attained maximum currents are far from those observed for optimized composite electrodes containing carbon substrates for the catalysts, e.g., Pt/C [45]. The ORR peak appeared at ca. 0.6 V for $\text{Ce}_{0.95}\text{Ni}_{0.05}\text{O}_{2-\delta}$ and $\text{Ce}_{0.80}\text{Ni}_{0.20}\text{O}_{2-\delta}$, except for $\text{Ce}_{0.85}\text{Ni}_{0.15}\text{O}_{2-\delta}$ (0.65 V) and $\text{Ce}_{0.90}\text{Ni}_{0.10}\text{O}_{2-\delta}$ (0.5 V). All $\text{Ce}_{1-x}\text{Ni}_x\text{O}_{2-\delta}$ samples gave ORR current densities of the same order of magnitude, in the -0.22 to -0.50 mA cm^{-2} range. The ORR peak current density tends to decrease with increasing Ni content in ceria, being the highest for $\text{Ce}_{0.95}\text{Ni}_{0.05}\text{O}_{2-\delta}$ (-0.50 mA cm^{-2}), followed by $\text{Ce}_{0.90}\text{Ni}_{0.10}\text{O}_{2-\delta}$ (-0.46 mA cm^{-2}) and $\text{Ce}_{0.80}\text{Ni}_{0.20}\text{O}_{2-\delta}$ (-0.42 mA cm^{-2}), while the lowest ORR current density was exceptionally recorded at $\text{Ce}_{0.85}\text{Ni}_{0.15}\text{O}_{2-\delta}$, (-0.22 mA cm^{-2}). These peak current densities are obtained after subtraction of the background current densities, i.e., the current densities recorded in deaerated electrolyte solution. These low currents may be justified by the overall low (in comparison to e.g., platinum) electronic conductivity of these phases, aggravated by the absence of a secondary conducting support such as carbon.

Tafel analysis of LSV data was performed and the Tafel slopes were evaluated from E vs. $\log j$ plots in the 0.57 – 0.78 V potential region (Figure 2B). The Tafel slope values were found to be 70 mV dec^{-1} for the electrode with the highest Ni content, $\text{Ce}_{0.80}\text{Ni}_{0.20}\text{O}_{2-\delta}$, and varying within 102 – 108 mV dec^{-1} for the other three electrodes, thus indicating a significant change in the rate-determining step of the ORR in the former case. The lower

value for $\text{Ce}_{0.80}\text{Ni}_{0.20}\text{O}_{2-\delta}$ may indicate a slightly different mechanism associated with NiO intervention, which exuded from the ceria lattice exceeding the Ni solubility limit and accounting for about 4% of the phase composition (see Table 1). Nevertheless, the Tafel slopes compare well with commercial Pt/C electrodes, which typically display Tafel slopes close to 80 mV dec^{-1} [45,46]. Comparison with the literature data reveals somewhat higher values for NiO/C and NiCoO₂/C, which show Tafel slope values of 112 and 149 mV dec^{-1} in the region of high current densities during ORR in alkaline media [47]. The Tafel slopes for ORR at NiO and CuO–NiO nanocomposites were found to be 90 and 204 mV dec^{-1} , respectively [48].

ORR at the Ni-doped CeO₂ samples was next investigated by LSV RDE method to evaluate the materials' faradaic efficiency for ORR. Thus, electrode potential was scanned at 10 mV s^{-1} , while electrode rotation rate ranged between 300 and 2400 rpm. The number of exchanged electrons, n , was then determined using the Koutecky–Levich equation (Equation (4)),

$$\frac{1}{j} = \frac{1}{j_d} + \frac{1}{j_k} = \frac{1}{0.62nF D_{\text{O}_2}^{2/3} \nu^{-1/6} C_{\text{bulk}} \omega^{1/2}} + \frac{1}{j_k} \quad (4)$$

where j_d and j_k are the diffusion-limited and kinetic current densities, respectively, ν is the kinematic viscosity of the solution ($\text{cm}^2 \text{ s}^{-1}$), F is Faraday's constant ($96,485 \text{ C mol}^{-1}$), D_{O_2} is the O₂ diffusion coefficient in 0.1 M KOH ($\text{cm}^2 \text{ s}^{-1}$), C_{bulk} is O₂ concentration (mol cm^{-3}). The n values were evaluated from the slope of j^{-1} vs. $\omega^{-1/2}$ plots (Figure 2C) and found to be 2.7 for ORR at $\text{Ce}_{0.95}\text{Ni}_{0.05}\text{O}_{2-\delta}$, 2.4 for $\text{Ce}_{0.90}\text{Ni}_{0.10}\text{O}_{2-\delta}$, 1.9 for $\text{Ce}_{0.80}\text{Ni}_{0.20}\text{O}_{2-\delta}$, and 1.6 for $\text{Ce}_{0.85}\text{Ni}_{0.15}\text{O}_{2-\delta}$ at the potential of 0.4 V. The obtained n values indicate that ORR at $\text{Ce}_{1-x}\text{Ni}_x\text{O}_{2-\delta}$ proceeds by $2e^-$ -pathway to HO₂[−]. The $2e^-$ -process might also be relevant for some fuel cell applications, as it offers the possibility of producing a useful chemical, i.e., H₂O₂, along with the generation of electricity [20].

Figure 2D shows the chronoamperograms recorded at 0.5 V of the four investigated materials in O₂-saturated KOH, indicating their stability in alkaline medium. After the typical initial decay for CA experiments, current densities stabilized after ca. 2 min at values around $-0.125 \text{ mA cm}^{-2}$, remaining relatively stable until the end of the experiments.

Figure 3A shows Nyquist plots of the four $\text{Ce}_{1-x}\text{Ni}_x\text{O}_{2-\delta}$ electrodes at a potential of 0.3 V and electrode rotation of 1200 rpm. The Nyquist plots of $\text{Ce}_{0.95}\text{Ni}_{0.05}\text{O}_{2-\delta}$ at 0.7, 0.5, and 0.3 V are shown in Figure 3B, with the high-frequency region in the inset. The plots depict the usual impedance contributions at high frequency, which may be ascribed to charge transfer kinetics, and another at lower frequency that results from mass transport diffusional limitations. Worth noting is the somewhat larger mass transport resistance of $\text{Ce}_{0.95}\text{Ni}_{0.05}\text{O}_{2-\delta}$, although there is no obvious reason for that based on the microstructural and compositional features presented in Table 1. Plots recorded at a potential of 0.7 V illustrate high charge transfer resistance of the 10^4 order of magnitude in the case of $\text{Ce}_{0.95}\text{Ni}_{0.05}\text{O}_{2-\delta}$. The highest resistance is observed for $\text{Ce}_{0.80}\text{Ni}_{0.20}\text{O}_{2-\delta}$, followed by $\text{Ce}_{0.85}\text{Ni}_{0.15}\text{O}_{2-\delta}$, while $\text{Ce}_{0.95}\text{Ni}_{0.05}\text{O}_{2-\delta}$ and $\text{Ce}_{0.90}\text{Ni}_{0.10}\text{O}_{2-\delta}$ showed the lowest resistance. This agrees with the CV results that showed ORR onset potentials of ca. 0.7 V, with the most positive onset potential value and highest peak current density recorded at $\text{Ce}_{0.95}\text{Ni}_{0.05}\text{O}_{2-\delta}$. Shifting the potential to less positive values, at which ORR proceeds at measurable rates, a significant decrease in resistance is observed.

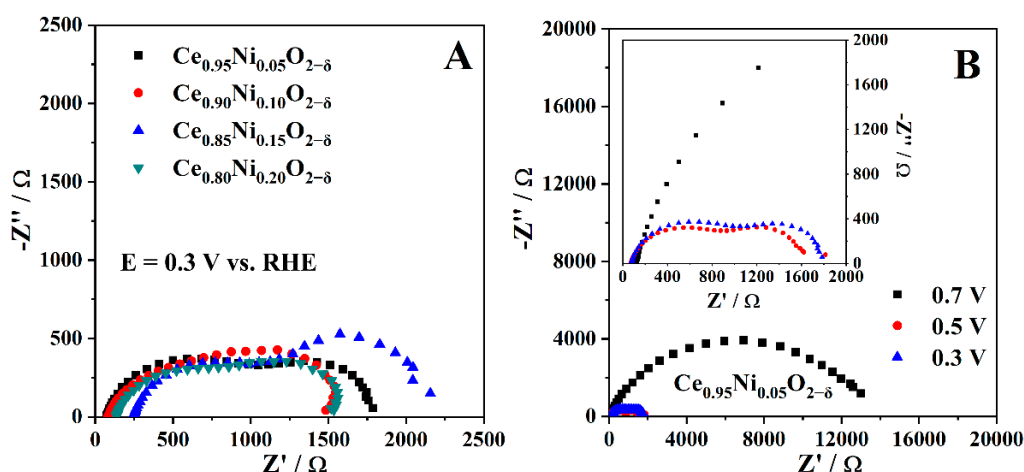


Figure 3. Nyquist plots of (A) $\text{Ce}_{0.95}\text{Ni}_{0.05}\text{O}_{2-\delta}$, $\text{Ce}_{0.90}\text{Ni}_{0.10}\text{O}_{2-\delta}$, $\text{Ce}_{0.85}\text{Ni}_{0.15}\text{O}_{2-\delta}$, and $\text{Ce}_{0.80}\text{Ni}_{0.20}\text{O}_{2-\delta}$ at a potential of 0.3 V and of (B) $\text{Ce}_{0.95}\text{Ni}_{0.05}\text{O}_{2-\delta}$ at potentials of 0.7, 0.5, and 0.3 V, with the high-frequency region in the inset. Potential values are corrected for the ohmic drop in the electrolyte. Measurements carried out in O_2 -saturated 0.1 M KOH solution and electrode rotation rate of 1200 rpm.

2.4. OER Studies

The OER study was carried out by first recording LSVs in the potential range from 1.2 to 2.2 V. Figure 4A shows that $\text{Ce}_{0.80}\text{Ni}_{0.20}\text{O}_{2-\delta}$, $\text{Ce}_{0.85}\text{Ni}_{0.15}\text{O}_{2-\delta}$, and $\text{Ce}_{0.90}\text{Ni}_{0.10}\text{O}_{2-\delta}$ electrocatalysts have similar OER onset potential values of ca. 1.58 V, while that of $\text{Ce}_{0.95}\text{Ni}_{0.05}\text{O}_{2-\delta}$ (1.65 V) is somewhat higher. These values are comparable with those reported in the literature for OER at other Ni-containing electrocatalysts (1.686–1.539 V for different Fe/Ni-N-doped carbon nanofibers) [9]. Overpotential necessary to drive current density of 1 mA cm^{-2} was found to be similar for $\text{Ce}_{0.80}\text{Ni}_{0.20}\text{O}_{2-\delta}$, $\text{Ce}_{0.85}\text{Ni}_{0.15}\text{O}_{2-\delta}$, and $\text{Ce}_{0.90}\text{Ni}_{0.10}\text{O}_{2-\delta}$ (ca. 560 mV), but notably higher in the case of $\text{Ce}_{0.95}\text{Ni}_{0.05}\text{O}_{2-\delta}$ (810 mV). OER current densities at potential of 2.0 V increased in the order $\text{Ce}_{0.95}\text{Ni}_{0.05}\text{O}_{2-\delta}$ (0.9 mA cm^{-2}) < $\text{Ce}_{0.90}\text{Ni}_{0.10}\text{O}_{2-\delta}$ (1.8 mA cm^{-2}) < $\text{Ce}_{0.85}\text{Ni}_{0.15}\text{O}_{2-\delta}$ (2.8 mA cm^{-2}) < $\text{Ce}_{0.80}\text{Ni}_{0.20}\text{O}_{2-\delta}$ (2.9 mA cm^{-2}).

LSV results were subsequently used to construct the Tafel plots and determine the Tafel slopes (inset of Figure 4A). The lowest Tafel slope values determined for OER were found for the two materials with higher Ni content ($\text{Ce}_{0.85}\text{Ni}_{0.15}\text{O}_{2-\delta}$ with 192 mV dec^{-1} , and $\text{Ce}_{0.80}\text{Ni}_{0.20}\text{O}_{2-\delta}$ with 206 mV dec^{-1}), while slopes for $\text{Ce}_{0.90}\text{Ni}_{0.10}\text{O}_{2-\delta}$ (232 mV dec^{-1}) and $\text{Ce}_{0.95}\text{Ni}_{0.05}\text{O}_{2-\delta}$ (281 mV dec^{-1}) are distinctively higher and confirming a clear trend to increase with decreasing Ni content, thus suggesting a positive effect of lattice Ni on the overall OER performance of ceria. These values are significantly lower than those reported for OER at some other Ni-based samples (799 mV dec^{-1} at NiCo_2O_4 -graphene hybrid [10] or comparable to $\text{CeO}_2/\text{Cu-MOF}$ electrocatalysts (200 mV dec^{-1} during OER in 1 M KOH [49]) but are considerably higher than the values for state-of-the-art catalysts such as the reference RuO_2 , for which typical Tafel slope is close to 50 mV dec^{-1} [7,50].

The influence of temperature on the OER at $\text{Ce}_{1-x}\text{Ni}_x\text{O}_{2-\delta}$ electrocatalysts was investigated by LSV measurements in 0.1 M KOH in the 25–85 °C temperature range. The OER current densities at the four materials significantly increase with temperature (Figure 4B). For instance, the OER current density at $\text{Ce}_{0.90}\text{Ni}_{0.10}\text{O}_{2-\delta}$ increases from ca. 3 mA cm^{-2} at 25 °C to ca. 21 mA cm^{-2} at 85 °C. These data were used for the calculation of the apparent activation energy for OER, E_a^{app} , using the Arrhenius equation (Equation (5)) [51],

$$\frac{\partial \log j}{\partial (1/T)} = \frac{E_a^{\text{app}}}{R} \quad (5)$$

where R is the universal gas constant ($8.314 \text{ JK}^{-1} \text{ mol}^{-1}$) [52]. There is no obvious compositional effect on E_a^{app} , which is lowest for $\text{Ce}_{0.85}\text{Ni}_{0.15}\text{O}_{2-\delta}$ (26 kJ mol^{-1}) followed by

$\text{Ce}_{0.95}\text{Ni}_{0.05}\text{O}_{2-\delta}$ and $\text{Ce}_{0.80}\text{Ni}_{0.20}\text{O}_{2-\delta}$ (31 kJ mol^{-1}), while $\text{Ce}_{0.90}\text{Ni}_{0.10}\text{O}_{2-\delta}$ shows the highest E_a^{app} value of 41 kJ mol^{-1} (inset of Figure 4B). For the sake of comparison, one notes that Ni, Ni-Co, and Ni-Fe alloys on mild steel substrates have E_a^{app} of 55 kJ mol^{-1} [53].

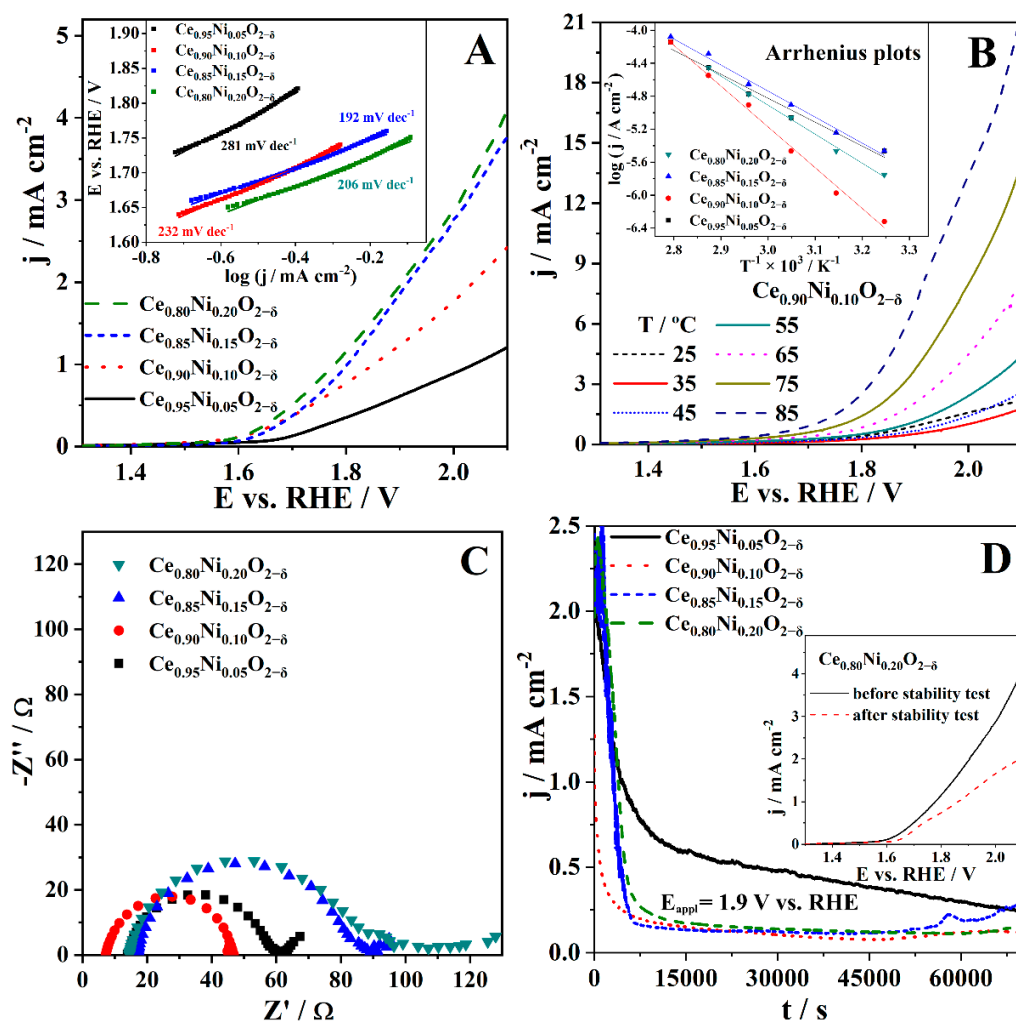


Figure 4. (A) RDE LSVs of the four studied $\text{Ce}_{1-x}\text{Ni}_x\text{O}_{2-\delta}$ electrocatalysts at 10 mV s^{-1} with corresponding Tafel slopes in inset. (B) Effect of temperature on the LSVs of $\text{Ce}_{0.90}\text{Ni}_{0.10}\text{O}_{2-\delta}$ at 10 mV s^{-1} in the $25\text{--}85 \text{ }^\circ\text{C}$ range with the Arrhenius plots of the four electrocatalysts in inset. (C) Nyquist plots of $\text{Ce}_{1-x}\text{Ni}_x\text{O}_{2-\delta}$ electrocatalysts at 2.2 V . (D) Chronoamperometric measurements at 1.9 V with LSVs recorded before and after the CA study in inset. Potential values are corrected for the ohmic drop in the electrolyte. All measurements performed in 0.1 M KOH electrolyte solution and $25 \text{ }^\circ\text{C}$, unless otherwise noted.

Nyquist plots of the four $\text{Ce}_{1-x}\text{Ni}_x\text{O}_{2-\delta}$ electrocatalysts were recorded in 0.1 M KOH at different potentials. Those recorded at 2.2 V are shown in Figure 4C. Compared to the ORR, the OER spectra display one dominant semicircle at high frequency, which suggests the charge-transfer resistance to be the most relevant to the overall OER performance of these electrodes [54]. As expected, a significant decrease in the semicircle amplitude is observed for increasing applied potential, which denotes a reduction in resistance and faster OER kinetics at these potentials.

Stability tests were performed for 20 h (Figure 4D). Current densities were observed to be relatively constant, except for $\text{Ce}_{0.95}\text{Ni}_{0.05}\text{O}_{2-\delta}$ where current density decay was observed. Polarization curves run after the stability test evidenced a decrease in the OER activity (inset of Figure 4D).

The stability of these materials in strongly alkaline conditions and under applied potentials cannot be avoided, namely the effects on the nickel solubility in the ceria lattice and all the concomitant phase changes resulting from this delicate equilibrium. One recalls that the achieved 15 at.% Ni solubility is only achieved in nanoparticles due to accommodation of excess energy by the surface (e.g., due to formation of hydroxides or dissolution of material leading to leaching of Ni and/or Ce cations), which means that even minor changes to the surface energy may have an impact on the phase stability. These are issues that must be addressed in future studies disclosing the potential of these interesting bifunctional electrocatalysts. Those will pave the way for the commercial application of $\text{Ce}_{1-x}\text{Ni}_x\text{O}_{2-\delta}$ nanopowders as bifunctional oxygen electrodes in rechargeable metal–air batteries, or other systems such as unitized regenerative fuel cells.

3. Materials and Methods

A detailed description of the synthesis by the cation complexation method and the characterization of the $\text{Ce}_{1-x}\text{Ni}_x\text{O}_{2-\delta}$ ($x = 0, 0.05, 0.10, 0.15,$ and 0.20) nanopowders are given in ref. [42] to own work, and thus a summary is presented here. The synthesis starts from aqueous solutions of $\text{Ce}(\text{NO}_3)_3 \cdot 6\text{H}_2\text{O}$ (99.99 wt.%, Alfa Aesar) and $\text{Ni}(\text{NO}_3)_2 \cdot 6\text{H}_2\text{O}$ (99.9 wt.%, Alfa Aesar) with the appropriate Ce:Ni molar ratios. A gel is then obtained upon addition of a citric acid solution, which is subsequently dried at $100\text{ }^\circ\text{C}$ for 20 min, fired at $250\text{ }^\circ\text{C}$ for 1 h and at $500\text{ }^\circ\text{C}$, again for 1 h, always in air, to obtain the desired oxide nanopowders. The physicochemical characterization of the prepared materials was carried out by a battery of methods, including conventional and synchrotron radiation X-ray diffraction, X-ray absorption near-edge spectroscopy (XANES), nitrogen sorption isotherms at 77 K, and transmission and scanning electron microscopies in high- and low-resolution modes, and coupled to energy dispersive spectroscopy (EDS). Synchrotron radiation X-ray diffraction (SR-XRD) patterns were recorded at room temperature using synchrotron radiation at the D10B-XPD beamline of the National Synchrotron Light Laboratory (LNLS, Campinas, Brazil). The X-ray wavelength was set at 1.55033 Å. Data in the angular range $2\theta = 20\text{--}85^\circ$ were collected in step-scanning mode, with a step length of 0.05° and a step-counting time of 4 s. NIST SRM 640c Si powder was used as the standard for the instrumental broadening correction. An extended summary of these results is presented in Section 2.1 of this paper, together with new Fourier transform infrared spectroscopy (FTIR) spectra collected using a Magna 550 Nicolet instrument equipped with CsI optics using the KBr pellets technique. All spectra were acquired at 4 cm^{-1} resolution and accumulation of 32 scans.

Catalytic inks were prepared by ultrasonically dispersing 5 mg of the corresponding $\text{Ce}_{1-x}\text{Ni}_x\text{O}_{2-\delta}$ electrocatalyst in 125 μL of 2 wt.% polyvinylidene difluoride solution in N-methyl 2-pyrrolidone for 30 min. The working electrodes were prepared by pipetting 10 μL of each catalytic ink onto glassy carbon (GC) supports and leaving it to dry at $100\text{ }^\circ\text{C}$. Current densities were calculated using the geometric area of GC supports.

All electrochemical measurements were performed using a Gamry PCI4/750 Potentiostat/Galvanostat in a one-compartment glass cell of 40 mL with graphite rod and saturated calomel electrode (SCE) serving as counter and reference electrodes, respectively. All potentials within this paper are given relative to the reversible hydrogen electrode, with the conversion being performed using the equation $E_{\text{RHE}} = E_{\text{SCE}} + 0.242 + 0.059\text{ pH}$.

CVs were first recorded in deaerated 0.1 M KOH (analytical reagent grade, Fisher Chemicals) using different scan rates in the $10\text{--}500\text{ mV s}^{-1}$ range. These CVs were used to determine the specific capacitance, C (F g^{-1}), according to Equation (6),

$$C = \frac{\int iE dE}{mv\Delta E} \quad (6)$$

where i is the current response, E is the potential, m is the mass of $\text{Ce}_{1-x}\text{Ni}_x\text{O}_{2-\delta}$ electrocatalyst on the GC support, v is the potential scan rate, and ΔE is the potential window.

For ORR studies, CVs were recorded in 0.1 M KOH solution saturated with O₂ (>99.999%, Messer, Bad Soden am Taunus, Germany), scanning the potential from 0.8 to 0.2 V at a scan rate of 50 mV s⁻¹. LSVs with RDE were recorded at a scan rate of 10 mV s⁻¹ and rotation rates ranging from 300 to 2400 rpm set by Pine AFCPRB rotator. CA measurements with the four studied materials were performed in the same O₂-saturated electrolyte solution at a constant potential of 0.5 V for 24 h. EIS measurements with the four electrode materials were carried out at potentials of 0.7, 0.5, and 0.3 V and a rotation rate of 1200 rpm in the frequency range of 0.01–100 kHz.

For OER studies, LSVs were run in 0.1 M KOH electrolyte solution from the open circuit potential (OCP) up to 2.2 V at scan rate of 10 mV s⁻¹. OER studies were performed in the 25–85 °C range using a Haake F3 thermostatic bath to control the solution temperature. OER EIS measurements were performed at different potential values (OCP, 1.30, 1.65, 1.95, and 2.20 V) at frequencies in the 0.01–100 kHz range. Stability in OER conditions was examined by chronoamperometry at 1.9 V for 20 h.

4. Conclusions

Four nickel-doped ceria (Ce_{1-x}Ni_xO_{2-δ}) nanopowders with different amounts of Ni were studied as bifunctional electrocatalysts for the ORR and OER in alkaline medium. Different electrochemical methods evaluated the Ce_{1-x}Ni_xO_{2-δ} nanopowders without adding any carbon materials to avoid contaminating the assessment of their intrinsic electrocatalytic activity. The specific capacitance of Ce_{1-x}Ni_xO_{2-δ} electrocatalysts was also evaluated, showing a behavior typical of electrolytic capacitors. All electrocatalysts showed activity for ORR, with Ce_{0.95}Ni_{0.05}O_{2-δ} showing the best performance in terms of highest peak current density, lowest Tafel slope, and highest number of exchanged electrons. ORR Tafel analysis performed in the 0.57–0.78 V potential window revealed Tafel slope values ranging from 70 to 108 mV dec⁻¹. The number of electrons exchanged during ORR was determined to range between 2 and 2.7. The OER Tafel slope values were in the 192–281 mV dec⁻¹ range, with improved OER performance being observed when increasing Ni content in the electrocatalysts. OER E_a^{app} values ranged from 26 kJ mol⁻¹ for Ce_{0.85}Ni_{0.15}O_{2-δ} to 41 kJ mol⁻¹ for Ce_{0.90}Ni_{0.10}O_{2-δ}. The bifunctional character of the studied Ce_{1-x}Ni_xO_{2-δ} nanopowders is particularly relevant for developing oxygen electrodes for application in more efficient rechargeable metal–air batteries.

Supplementary Materials: The following supporting information can be downloaded at: <https://www.mdpi.com/article/10.3390/batteries8080100/s1>, Figure S1: Synchrotron radiation powder X-ray diffraction (SR-XRD) patterns recorded at room temperature for the nanostructured Ce_{1-x}Ni_xO_{2-δ} materials; Figure S2: Fourier transform infrared spectra (FTIR) spectra of the Ce_{1-x}Ni_xO_{2-δ} nanopowders; Figure S3: Low-resolution scanning transmission electron microscopy (STEM) image of the Ce_{0.90}Ni_{0.10}O_{2-δ} sample obtained on a Scanning Electron Microscope equipped with a transmission detector (Hitachi SU 70); Figure S4: Pore size distribution for the Ce_{1-x}Ni_xO_{2-δ} nanopowders estimated from the nitrogen desorption data using the Barrett–Joyner–Halenda method utilizing the Halsey thickness curve with the G.S. Faass correction; Figure S5: Cyclic voltammograms of Ce_{0.95}Ni_{0.05}O_{2-δ} in deaerated 0.1 M KOH electrolyte solution at scan rates ranging from 10 to 500 mV s⁻¹; Figure S6: Voltammetric response of Ce_{0.95}Ni_{0.05}O_{2-δ} in deaerated and O₂-saturated 0.1 M KOH.

Author Contributions: Conceptualization, F.M.L.F., R.O.F., D.M.F.S. and B.Š.; Formal analysis, J.M.; Funding acquisition, F.M.L.F., R.O.F., D.M.F.S. and B.Š.; Investigation, J.M., J.E.T., R.O.F., F.M.L.F., D.M.F.S. and B.Š.; Project administration, D.M.F.S. and F.M.L.F.; Supervision, R.O.F., F.M.L.F., D.M.F.S. and B.Š.; Validation, J.E.T. and R.O.F.; Visualization, J.M., D.M.F.S. and B.Š.; Writing—original draft, J.M.; Writing—review and editing, D.M.F.S., F.M.L.F. and B.Š. All authors have read and agreed to the published version of the manuscript.

Funding: The authors would like to thank to the Ministry of Education, Science and Technological Development of Republic of Serbia for support within project no. OI172043, and the Science and Technological cooperation agreement MINCYT (Argentina)—MEC (Portugal), Project PO/14/04. Fundação para a Ciência e a Tecnologia (FCT, Portugal) is acknowledged for funding a research contract in the scope of programmatic funding UIDP/04540/2020 (D.M.F.S.) and contract no. IST-ID/156-2018 (B.S.).

This work was also developed within the scope of the projects UniRCell (SAICTPAC/0032/2015, POCI-01-0145-FEDER-016422), financed by national funds through the FCT/MEC, and CICECO Aveiro Institute of Materials UIDB/50011/2020, UIDP/50011/2020, and LA/P/0006/2020, financed by national funds through the FCT/MEC (PIDDAC).

Data Availability Statement: The data presented in this study are available on request from the corresponding author.

Conflicts of Interest: The authors declare no conflict of interest. The funders had no role in the design of the study; in the collection, analyses, or interpretation of data; in the writing of the manuscript, or in the decision to publish the results.

References

1. Ralph, T.R.; Hogarth, M.P. Catalysis for low temperature fuel cells. *Platin. Met. Rev.* **2002**, *46*, 117–135. [[CrossRef](#)]
2. Mota, N.D.; Finkelstein, I.D.; Kirtland, I.J.D.; Claudia, I.; Stroock, A.D.; Abruña, H.D. Membraneless, Room-Temperature, Direct Borohydride/Cerium Fuel Cell with Power Density of Over 0.25 W cm^{-2} . *J. Am. Chem. Soc.* **2012**, *134*, 6076–6079. [[CrossRef](#)] [[PubMed](#)]
3. Wang, Y.G.; Xia, Y.Y. A direct borohydride fuel cell using MnO_2 -catalyzed cathode and hydrogen storage alloy anode. *Electrochem. Commun.* **2006**, *8*, 1775–1778. [[CrossRef](#)]
4. Liu, J.; Zhao, Q.; Wu, C.; Wang, Y.; Wei, W.; Wang, X.; Yi, L. Performance improvement of activated nanoporous carbon supported gold catalyst as an anode for direct borohydride–hydrogen peroxide fuel cells. *RSC Adv.* **2014**, *4*, 17129–17135. [[CrossRef](#)]
5. Ma, J.; Liu, Y.; Zhang, P.; Wang, J. A simple direct borohydride fuel cell with a cobalt phthalocyanine catalyzed cathode. *Electrochem. Commun.* **2008**, *10*, 100–102. [[CrossRef](#)]
6. Šljukić, B.; Santos, D.M.F.; Sequeira, C.A.C. Manganese dioxide electrocatalysts for borohydride fuel cell cathodes? *J. Electroanal. Chem.* **2013**, *694*, 77–83. [[CrossRef](#)]
7. Reier, T.; Oezaslan, M.; Strasser, P. Electrocatalytic oxygen evolution reaction (OER) on Ru, Ir, and Pt catalysts: A comparative study of nanoparticles and bulk materials. *ACS Catal.* **2012**, *2*, 1765–1772. [[CrossRef](#)]
8. Mosiałek, M.; Nowak, P.; Dudek, M.; Mordarski, G. Oxygen reduction at the $\text{Ag}|\text{Gd}_{0.2}\text{Ce}_{0.8}\text{O}_{1.9}$ interface studied by electrochemical impedance spectroscopy and cyclic voltammetry at the silver point electrode. *Electrochim. Acta* **2014**, *120*, 248–257. [[CrossRef](#)]
9. Wang, Z.; Li, M.; Fan, L.; Han, J.; Xiong, Y. Fe/Ni-N-CNFs electrochemical catalyst for oxygen reduction reaction/oxygen evolution reaction in alkaline media. *Appl. Surf. Sci.* **2017**, *401*, 89–99. [[CrossRef](#)]
10. Lee, D.U.; Kim, B.J.; Chen, Z. One-pot synthesis of a mesoporous NiCo_2O_4 nanoplatelet and graphene hybrid and its oxygen reduction and evolution activities as an efficient bi-functional electrocatalyst. *J. Mater. Chem. A* **2013**, *1*, 4754. [[CrossRef](#)]
11. Choi, B.; Lee, S.; Fushimi, C.; Tsutsumi, A. Development of NiMH-based Fuel Cell/Battery (FCB) system: Characterization of $\text{Ni}(\text{OH})_2/\text{MnO}_2$ positive electrode for FCB. *J. Power Sources* **2009**, *194*, 1150–1155. [[CrossRef](#)]
12. Dar, Y.R.; Vijay, P.; Tade, M.O.; Datta, R. Topological analysis of hydrogen oxidation reaction kinetics at Ni/YSZ anode of the solid oxide fuel cell. *J. Electroanal. Chem.* **2012**, *677–680*, 15–23. [[CrossRef](#)]
13. Chen, Z.; Yu, A.; Higgins, D.; Li, H.; Wang, H.; Chen, Z. Highly active and durable core-corona structured bifunctional catalyst for rechargeable metal-air battery application. *Nano Lett.* **2012**, *12*, 1946–1952. [[CrossRef](#)]
14. Lee, J.S.; Kim, S.T.; Cao, R.; Choi, N.S.; Liu, M.; Lee, K.T.; Cho, J. Metal-air batteries with high energy density: Li-air versus Zn-air. *Adv. Energy Mater.* **2011**, *1*, 34–50. [[CrossRef](#)]
15. Zhang, J.; Zhao, Z.; Xia, Z.; Dai, L. A metal-free bifunctional electrocatalyst for oxygen reduction and oxygen evolution reactions. *Nat. Nanotechnol.* **2015**, *10*, 444–452. [[CrossRef](#)] [[PubMed](#)]
16. Bing, Y.; Liu, H.; Zhang, L.; Ghosh, D.; Zhang, J. Nanostructured Pt-alloy electrocatalysts for PEM fuel cell oxygen reduction reaction. *Chem. Soc. Rev.* **2010**, *39*, 2184. [[CrossRef](#)]
17. Higgins, D.C.; Meza, D.; Chen, Z. Nitrogen-Doped Carbon Nanotubes as Platinum Catalyst Supports for Oxygen Reduction Reaction in Proton Exchange Membrane Fuel Cells. *J. Phys. Chem. C* **2010**, *114*, 21982–21988. [[CrossRef](#)]
18. Gasteiger, H.A.; Kocha, S.S.; Sompalli, B.; Wagner, F.T. Activity benchmarks and requirements for Pt, Pt-alloy, and non-Pt oxygen reduction catalysts for PEMFCs. *Appl. Catal. B Environ.* **2005**, *56*, 9–35. [[CrossRef](#)]
19. Schulze, M.; Wagner, N.; Kaz, T.; Friedrich, K.A. Combined electrochemical and surface analysis investigation of degradation processes in polymer electrolyte membrane fuel cells. *Electrochim. Acta* **2007**, *52*, 2328–2336. [[CrossRef](#)]
20. Sheng, X.; Daems, N.; Geboes, B.; Kurttepli, M.; Bals, S.; Breugelmans, T.; Hubin, A.; Vankelecom, I.F.J.; Pescarmona, P.P. N-doped ordered mesoporous carbons prepared by a two-step nanocasting strategy as highly active and selective electrocatalysts for the reduction of O_2 to H_2O_2 . *Appl. Catal. B Environ.* **2015**, *176–177*, 212–224. [[CrossRef](#)]
21. Meng, Y.; Song, W.; Huang, H.; Ren, Z.; Chen, S.; Suib, S.L. Structure-Property Relationship of Bifunctional MnO_2 Nanostructures: Highly Efficient, Ultra-Stable Electrochemical Water Oxidation and Oxygen Reduction Reaction Catalysts Identified in Alkaline Media. *J. Am. Chem. Soc.* **2014**, *136*, 11452–11464. [[CrossRef](#)] [[PubMed](#)]
22. Tseung, A.C.C.; Jasem, S. Oxygen evolution on semiconducting oxides. *Electrochim. Acta* **1977**, *22*, 31–34. [[CrossRef](#)]

23. Lyons, M.E.G.; Brandon, M.P. A comparative study of the oxygen evolution reaction on oxidised nickel, cobalt and iron electrodes in base. *J. Electroanal. Chem.* **2010**, *641*, 119–130. [[CrossRef](#)]
24. Jin, H.; Yu, H.; Li, H.; Davey, K.; Song, T.; Paik, U.; Qiao, S.-Z. MXene Analogue: A 2D Nitridene Solid Solution for High-Rate Hydrogen Production. *Angew. Chem. Int. Ed.* **2022**, *61*, e202203850. [[CrossRef](#)]
25. Jin, H.; Song, T.; Paik, U.; Qiao, S.-Z. Metastable Two-Dimensional Materials for Electrocatalytic Energy Conversions. *Acc. Mater. Res.* **2021**, *2*, 559–573. [[CrossRef](#)]
26. Zhang, Z.; Liu, J.; Gu, J.; Su, L.; Cheng, L. An overview of metal oxide materials as electrocatalysts and supports for polymer electrolyte fuel cells. *Energy Environ. Sci.* **2014**, *7*, 2535–2558. [[CrossRef](#)]
27. Deng, J.; Chu, W.; Wang, B.; Yang, W.; Zhao, X.S. Mesoporous Ni/Ce_{1-x}Ni_xO_{2-y} heterostructure as an efficient catalyst for converting greenhouse gas to H₂ and syngas. *Catal. Sci. Technol.* **2016**, *6*, 851–862. [[CrossRef](#)]
28. Shan, W.; Luo, M.; Ying, P.; Shen, W.; Li, C. Reduction property and catalytic activity of Ce_{1-x}Ni_xO₂ mixed oxide catalysts for CH₄ oxidation. *Appl. Catal. A Gen.* **2003**, *246*, 1–9. [[CrossRef](#)]
29. Zhou, G.; Barrio, L.; Agnoli, S.; Senanayake, S.D.; Evans, J.; Kubacka, A.; Estrella, M.; Hanson, J.C.; Martínez-Arias, A.; Fernández-García, M.; et al. High activity of Ce_{1-x}Ni_xO_{2-y} for H₂ production through ethanol steam reforming: Tuning catalytic performance through metal-oxide interactions. *Angew. Chem. Int. Ed.* **2010**, *49*, 9680–9684. [[CrossRef](#)] [[PubMed](#)]
30. Elias, J.S.; Risch, M.; Giordano, L.; Mansour, A.N.; Shao-Horn, Y. Structure, bonding, and catalytic activity of monodisperse, transition-metal-substituted CeO₂ nanoparticles. *J. Am. Chem. Soc.* **2014**, *136*, 17193–17200. [[CrossRef](#)]
31. Barrio, L.; Kubacka, A.; Zhou, G.; Estrella, M.; Martínez-Arias, A.; Hanson, J.C.; Fernández-García, M.; Rodríguez, J.A. Unusual Physical and Chemical Properties of Ni in Ce_{1-x}Ni_xO_{2-y} Oxides: Structural Characterization and Catalytic Activity for the Water Gas Shift Reaction. *J. Phys. Chem. C* **2010**, *114*, 12689–12697. [[CrossRef](#)]
32. Tao, Z.; Hou, G.; Xu, N.; Zhang, Q. A highly coking-resistant solid oxide fuel cell with a nickel doped ceria: Ce_{1-x}Ni_xO_{2-y} reformation layer. *Int. J. Hydrogen Energy* **2014**, *39*, 5113–5120. [[CrossRef](#)]
33. Tan, Q.; Du, C.; Sun, Y.; Du, L.; Yin, G.; Gao, Y. Nickel-doped ceria nanoparticles for promoting catalytic activity of Pt/C for ethanol electrooxidation. *J. Power Sources* **2014**, *263*, 310–314. [[CrossRef](#)]
34. Parwaiz, S.; Bhunia, K.; Das, A.K.; Khan, M.M.; Pradhan, D. Cobalt-Doped Ceria/Reduced Graphene Oxide Nanocomposite as an Efficient Oxygen Reduction Reaction Catalyst and Supercapacitor Material. *J. Phys. Chem. C* **2017**, *121*, 20165–20176. [[CrossRef](#)]
35. Yang, Z.-B.; Yue, T.-L.; Yu, X.-N.; Wu, M.-M. Electrocatalytic Activity of Cobalt Doped Ceria Nanoparticles. *J. Inorg. Mater.* **2018**, *33*, 845–853.
36. Meléndez-González, P.C.; Sánchez-Castro, E.; Alonso-Lemus, I.L.; Pérez-Hernández, R.; Escobar-Morales, B.; Garay-Tapia, A.M.; Pech-Rodríguez, W.J.; Rodríguez-Varela, J. Bifunctional Pd-CeO₂ Nanorods/C Nanocatalyst with High Electrochemical Stability and Catalytic Activity for the ORR and EOR in Alkaline Media. *ChemistrySelect* **2020**, *5*, 14032–14040. [[CrossRef](#)]
37. Sridharan, M.; Maiyalagan, T. Enhanced oxygen reduction activity of bimetallic Pd-Ag alloy-supported on mesoporous cerium oxide electrocatalysts in alkaline media. *New J. Chem.* **2021**, *45*, 22181–22192. [[CrossRef](#)]
38. Xu, S.; Lv, C.; He, T.; Huang, Z.; Zhang, C. Amorphous film of cerium doped cobalt oxide as a highly efficient electrocatalyst for oxygen evolution reaction. *J. Mater. Chem. A* **2019**, *7*, 7526–7532. [[CrossRef](#)]
39. Bhuvanendran, N.; Ravichandran, S.; Kandasamy, S.; Zhang, W.; Xu, Q.; Khotseng, L.; Maiyalagan, T.; Su, H. Spindle-shaped CeO₂/biochar carbon with oxygen-vacancy as an effective and highly durable electrocatalyst for oxygen reduction reaction. *Int. J. Hydrogen Energy* **2021**, *46*, 2128–2142. [[CrossRef](#)]
40. Yu, H.; Davydova, E.S.; Ash, U.; Miller, H.A.; Bonville, L.; Dekel, D.R.; Maric, R. Palladium-ceria nanocatalyst for hydrogen oxidation in alkaline media: Optimization of the Pd–CeO₂ interface. *Nano Energy* **2019**, *57*, 820–826. [[CrossRef](#)]
41. Kuzmanović, B.; Vujković, M.J.; Tomić, N.; Bajuk-Bogdanović, D.; Lazović, V.; Šljukić, B.; Ivanović, N.; Mentus, S. The influence of oxygen vacancy concentration in nanodispersed non-stoichiometric CeO_{2-δ} oxides on the physico-chemical properties of conducting polyaniline/CeO₂ composites. *Electrochim. Acta* **2019**, *306*, 506–515. [[CrossRef](#)]
42. Fuentes, R.O.; Acuña, L.M.; Albornoz, C.A.; Leyva, A.G.; Sousa, N.; Figueiredo, F.M. Structural, physical and chemical properties of nanostructured nickel-substituted ceria oxides under reducing and oxidizing conditions. *RSC Adv.* **2016**, *6*, 64861–64870. [[CrossRef](#)]
43. Shannon, R.D. Application of the Periodic Bond Chain (PBC) Theory and Attachment Energy Consideration to Derive the Crystal Morphology of Hexamethylmelamine. *Acta Crystallogr.* **1976**, *A32*, 751–767. [[CrossRef](#)]
44. Mentus, S.; Vujković, M.; Gavrilov, N.; Pašti, I.; Krstić, J.; Travas-Sejdic, J.; Ćirić-Marjanović, G. Superior capacitive and electrocatalytic properties of carbonized nanostructured polyaniline upon a low-temperature hydrothermal treatment. *Carbon* **2013**, *64*, 472–486. [[CrossRef](#)]
45. Zhang, C.; Shen, X.; Pan, Y.; Peng, Z. A review of Pt-based electrocatalysts for oxygen reduction reaction. *Front. Energy* **2017**, *11*, 268–285. [[CrossRef](#)]
46. Qiu, K.; Chai, G.; Jiang, C.; Ling, M.; Tang, J.; Guo, Z. Highly Efficient Oxygen Reduction Catalysts by Rational Synthesis of Nanoconfined Maghemite in a Nitrogen-Doped Graphene Framework. *ACS Catal.* **2016**, *6*, 3558–3568. [[CrossRef](#)]
47. Ashok, A.; Kumar, A.; Ponraj, J.; Mansour, S.A.; Tarlochan, F. Highly active and stable bi-functional NiCoO₂ catalyst for oxygen reduction and oxygen evolution reactions in alkaline medium. *Int. J. Hydrogen Energy* **2019**, *44*, 16603–16614. [[CrossRef](#)]

48. Sandhiran, N.; Ganapathy, S.; Manoharan, Y.; Ganguly, D.; Kumar, M.; Ramanujam, K.; Balachandran, S. CuO–NiO binary transition metal oxide nanoparticle anchored on rGO nanosheets as high-performance electrocatalyst for the oxygen reduction reaction. *Environ. Res.* **2022**, *211*, 112992. [[CrossRef](#)]
49. Chen, Y.; Huang, N.; Liang, Y. Preparation of CeO₂/Cu-MOF/GO composite for efficient electrocatalytic oxygen evolution reaction. *Ionics* **2021**, *27*, 4347–4360. [[CrossRef](#)]
50. Plevová, M.; Hnát, J.; Bouzek, K. Electrocatalysts for the oxygen evolution reaction in alkaline and neutral media. A comparative review. *J. Power Sources* **2021**, *507*. [[CrossRef](#)]
51. Milikić, J.; Ćirić-Marjanović, G.; Mentus, S.; Santos, D.M.F.; Sequeira, C.A.C.; Šljukić, B. Pd/c-PANI electrocatalysts for direct borohydride fuel cells. *Electrochim. Acta* **2016**, *213*, 298–305. [[CrossRef](#)]
52. Liu, D.M.; Huang, W.J.; Si, T.Z.; Zhang, Q.A. Hydrogen storage properties of LiBH₄ destabilized by SrH₂. *J. Alloy. Compd.* **2013**, *551*, 8–11. [[CrossRef](#)]
53. Suffredini, H.B.; Cerne, J.L.; Crnkovic, F.C.; Machado, S.A.S.; Avaca, L.A. Recent developments in electrode materials for water electrolysis. *Int. J. Hydrogen Energy* **2000**, *25*, 415–423. [[CrossRef](#)]
54. Lu, B.; Cao, D.; Wang, P.; Wang, G.; Gao, Y. Oxygen evolution reaction on Ni-substituted Co₃O₄ nanowire array electrodes. *Int. J. Hydrogen Energy* **2011**, *36*, 72–78. [[CrossRef](#)]